Research Article | Vol. 7, No. 10 | 1 Oct 2016 | BIOMEDICAL OPTICS EXPRESS 3968
Biomedical Optics EXPRESS

In vivo volumetric fluorescence sectioning microscopy with mechanical-scan-free hybrid illumination imaging

CHEN-YEN LIN,[1,2] WEI-HSIN LIN,[2,3] JU-HSUAN CHIEN,[2] JUI-CHANG TSAI,[2] AND YUAN LUO[2,4,*]

[1]*Department of Electrical Engineering and Graduate Institute of Photonics and Optoelectronics, National Taiwan University, Taipei 10617, Taiwan*
[2]*Institute of Medical Device and Imaging, National Taiwan University, Taipei, 10051, Taiwan*
[3]*School of Medicine, National Taiwan University, Taipei, 10051, Taiwan*
[4]*Molecular Imaging Center, National Taiwan University, Taipei 10055, Taiwan*
[*]*yuanluo@ntu.edu.tw*

Abstract: Optical sectioning microscopy in wide-field fashion has been widely used to obtain three-dimensional images of biological samples; however, it requires scanning in depth and considerable time to acquire multiple depth information of a volumetric sample. In this paper, *in vivo* optical sectioning microscopy with volumetric hybrid illumination, with no mechanical moving parts, is presented. The proposed system is configured such that the optical sectioning is provided by hybrid illumination using a digital micro-mirror device (DMD) for uniform and non-uniform pattern projection, while the depth of imaging planes is varied by using an electrically tunable-focus lens with invariant magnification and resolution. We present and characterize the design, implementation, and experimentally demonstrate the proposed system's ability through 3D imaging of *in vivo* Canenorhabditis elegans' growth cones.

OCIS codes: (110.0110) Imaging systems; (180.2520) Fluorescence microscopy; (110.6880) Three-dimensional image acquisition.

References and links

1. J. A. Conchello and J. W. Lichtman, "Optical sectioning microscopy," Nat. Methods **2**(12), 920–931 (2005).
2. C. J. R. Sheppard and A. Choudhury, "Image formation in the scanning microscope," Opt. Acta (Lond.) **24**(10), 1051–1073 (1977).
3. T. Wilson, "Resolution and optical sectioning in the confocal microscope," J. Microsc. **244**(2), 113–121 (2011).
4. M. A. A. Neil, R. Juškaitis, and T. Wilson, "Method of obtaining optical sectioning by using structured light in a conventional microscope," Opt. Lett. **22**(24), 1905–1907 (1997).
5. J. Mertz, "Optical sectioning microscopy with planar or structured illumination," Nat. Methods **8**(10), 811–819 (2011).
6. T. Fukano and A. Miyawaki, "Whole-Field Fluorescence Microscope with Digital Micromirror Device: Imaging of Biological Samples," Appl. Opt. **42**(19), 4119–4124 (2003).
7. P. Křížek, I. Raška, and G. M. Hagen, "Flexible structured illumination microscope with a programmable illumination array," Opt. Express **20**(22), 24585–24599 (2012).
8. L. H. Schaefer, D. Schuster, and J. Schaffer, "Structured illumination microscopy: artefact analysis and reduction utilizing a parameter optimization approach," J. Microsc. **216**(2), 165–174 (2004).
9. D. Lim, T. N. Ford, K. K. Chu, and J. Mertz, "Optically sectioned in vivo imaging with speckle illumination HiLo microscopy," J. Biomed. Opt. **16**(1), 016014 (2011).
10. H. H. Chen, V. R. Singh, and Y. Luo, "Speckle-based volume holographic microscopy for optically sectioned multi-plane fluorescent imaging," Opt. Express **23**(6), 7075–7084 (2015).
11. J. Rosen and G. Brooker, "Non-scanning motionless fluorescence three-dimensional holographic microscopy," Nat. Photonics **2**(3), 190–195 (2008).
12. P. A. Dalgarno, H. I. C. Dalgarno, A. Putoud, R. Lambert, L. Paterson, D. C. Logan, D. P. Towers, R. J. Warburton, and A. H. Greenaway, "Multiplane imaging and three dimensional nanoscale particle tracking in biological microscopy," Opt. Express **18**(2), 877–884 (2010).
13. S. Abrahamsson, J. Chen, B. Hajj, S. Stallinga, A. Y. Katsov, J. Wisniewski, G. Mizuguchi, P. Soule, F. Mueller, C. Dugast Darzacq, X. Darzacq, C. Wu, C. I. Bargmann, D. A. Agard, M. Dahan, and M. G. L. Gustafsson, "Fast multicolor 3D imaging using aberration-corrected multifocus microscopy," Nat. Methods **10**(1), 60–63 (2012).

#270407 http://dx.doi.org/10.1364/BOE.7.003968
Journal © 2016 Received 13 Jul 2016; revised 20 Aug 2016; accepted 20 Aug 2016; published 12 Sep 2016

Biomedical Optics EXPRESS

14. W. Liu, D. Psaltis, and G. Barbastathis, "Real-time spectral imaging in three spatial dimensions," Opt. Lett. **27**(10), 854–856 (2002).
15. L. Waller, Y. Luo, S.-Y. Yang, and G. Barbastathis, "Transport of intensity phase imaging in a volume holographic microscope," Opt. Lett. **35**(17), 2961–2963 (2010).
16. X. Zhai, W. T. Lin, H. H. Chen, P. H. Wang, L. H. Yeh, J. C. Tsai, V. R. Singh, and Y. Luo, "In-line digital holographic imaging in volume holographic microscopy," Opt. Lett. **40**(23), 5542–5545 (2015).
17. Y. Luo, V. R. Singh, D. Bhattacharya, E. Y. S. Yew, J.-C. Tsai, S.-L. Yu, H.-H. Chen, J.-M. Wong, P. Matsudaira, P. T. C. So, and G. Barbastathis, "Talbot holographic illumination nonscanning (THIN) fluorescence microscopy," Laser Photonics Rev. **8**(5), L71–L75 (2014).
18. J. M. Jabbour, B. H. Malik, C. Olsovsky, R. Cuenca, S. Cheng, J. A. Jo, Y.-S. L. Cheng, J. M. Wright, and K. C. Maitland, "Optical axial scanning in confocal microscopy using an electrically tunable lens," Biomed. Opt. Express **5**(2), 645–652 (2014).
19. F. O. Fahrbach, F. F. Voigt, B. Schmid, F. Helmchen, and J. Huisken, "Rapid 3D light-sheet microscopy with a tunable lens," Opt. Express **21**(18), 21010–21026 (2013).
20. T. Hinsdale, B. H. Malik, C. Olsovsky, J. A. Jo, and K. C. Maitland, "Volumetric structured illumination microscopy enabled by a tunable-focus lens," Opt. Lett. **40**(21), 4943–4946 (2015).
21. K. Philipp, A. Smolarski, N. Koukourakis, A. Fischer, M. Stürmer, U. Wallrabe, and J. W. Czarske, "Volumetric HiLo microscopy employing an electrically tunable lens," Opt. Express **24**(13), 15029–15041 (2016).
22. S. Santos, K. K. Chu, D. Lim, N. Bozinovic, T. N. Ford, C. Hourtoule, A. C. Bartoo, S. K. Singh, and J. Mertz, "Optically sectioned fluorescence endomicroscopy with hybrid-illumination imaging through a flexible fiber bundle," J. Biomed. Opt. **14**(3), 030502 (2009).
23. N. Bozinovic, C. Ventalon, T. Ford, and J. Mertz, "Fluorescence endomicroscopy with structured illumination," Opt. Express **16**(11), 8016–8025 (2008).
24. A. Masson, M. Pedrazzani, S. Benrezzak, P. Tchenio, T. Preat, and D. Nutarelli, "Micromirror structured illumination microscope for high-speed in vivo drosophila brain imaging," Opt. Express **22**(2), 1243–1256 (2014).
25. J. E. Greivenkamp, Field Guide to Geometrical Optics (SPIE, 2004)
26. P. J. Gelsinger-Austin, Y. Luo, J. M. Watson, R. K. Kostuk, G. Barbastathis, J. K. Barton, and J. M. Castro, "Optical design for a spatial-spectral volume holographic imaging system," Opt. Eng. **49**(4), 043001 (2010).
27. C. Y. Lin, W. T. Lin, H. H. Chen, J. M. Wong, V. R. Singh, and Y. Luo, "Talbot multi-focal holographic fluorescence endoscopy for optically sectioned imaging," Opt. Lett. **41**(2), 344–347 (2016).
28. K. M. Knobel, E. M. Jorgensen, and M. J. Bastiani, "Growth cones stall and collapse during axon outgrowth in Caenorhabditis elegans," Development **126**(20), 4489–4498 (1999).
29. J. Braat, "Analytical expressions for the wave-front aberration coefficients of a tilted plane-parallel plate," Appl. Opt. **36**(32), 8459–8467 (1997).

1. Introduction

In vivo laser-induced fluorescence imaging of a volumetric tissue sample is one of the most invaluable apparatuses to directly visualize mechanisms and processes within a biological sample. The use of the term "volumetric imaging" typically implies sectioning ability, so that truly *in vivo* 3D image data can be acquired, ideally in real time or at least at video rate. Standard wide-field fluorescence microscopy is a commonly used imaging technique by researchers and clinicians, but a standard wide-field microscope has no optical sectioning capabilities, which limits its use in imaging thick biological samples. Many recent improvements in optical microscopy have been centered on optical sectioning techniques [1–4]. For example, in confocal scanning microscopy [2, 3], fluorescence is excited by a focused beam and a pinhole at the image conjugate of the illumination rejects out-of-focus light. The price to pay for background rejection in confocal microscopy is scanning time in lateral dimensions as well as depth focusing, which is proportional to the resolution and scanning volume.

Compared with the laser scanning confocal microscopy, structured illumination microscopy (SIM) based on the wide-field fashion requires less light power and shorter acquisition time [5–7]. SIM obtains an optically sectioned image at one depth using computational reconstruction algorithms after three images are acquired by translating a grid for three different phases at a step of one third of a grid period. Although it could be a simpler and more cost effective than confocal techniques, it still needs an axial scanning and has difficulty to avoid mis-registration and artifact in final processed images [8]. The most recent improvements include hybrid illumination microscopy, which can be thought as more general

Biomedical Optics EXPRESS

than SIM imaging and can be also implemented with any type of non-uniform illumination of a particular pattern [9, 10].

To reduce or eliminate mechanical scanning, holography and diffraction gratings have been proposed in a variety of three-dimensional (3D) imaging techniques on the biological applications [11–15]. The most recent methods include Fresnel incoherent correlation holography (FINCH) [11], distorted thin gratings (QTG) [12, 13] and multiplex volume holography (MVH) [14, 15]. FINCH based on digital holographic microcopy (DHM) replaces scanning with deconvolution of the coherent Fresnel propagation kernel at multiple depths along the sample, but it does not yield true 3D images except in the limit of a sparsely populated object and it is not applicable for thick tissue [11]. Both QTG gratings and MVH simultaneously acquires multi-depth images of a biological sample. The former method does not offer fine scan step, and needs additional axial scanning to obtain images between depths [12, 13]. MVH can adopt DHM to enhance contrast of a sparsely populated sample [16], or incorporate structured illumination to provide fine optical sectioning with additional mechanical scanning among different layers [17].

Recently, focus tunable lens (FTL) for electrically high-speed focus adjustment has been utilized to eliminate mechanical moving parts in microscopy, including confocal microscopy [18], light sheet microscopy [19], and SIM [20]. Light sheet microscopy with FTL in detection may reduce scanning in depth, but it does not completely eliminate mechanical scanning in illumination. In the latter SIM, objective incorporating an FTL with magnification change for *ex vivo* imaging has been demonstrated, but it still needs to mechanically translate a grid for three different phases. In addition, it requires additional complicated imaging process since lateral resolution and contrast degrade due to variant magnification for each depth including the similar system recently being reported in [21].

Here, we experimentally demonstrate an *in vivo*, mechanical-scan-free, high-resolution, wide-field optically sectioned microscope for 3D volumetric imaging of biological samples, where contrast and speed are achieved from a combination of digital micro-mirror device (DMD) based hybrid illumination imaging and FTL with invariant magnification formation in fluorescent imaging. The parallelism allowing the complete elimination of mechanical scanning under constant magnification and contrast is provided by the FTL in detection in a telecentric fashion, while the active DMD based hybrid structured illumination provides depth contrast and suppression of scattered light. Therefore, our approach does not require any mechanical moving parts for *in vivo* 3D biopsy of a biological sample.

In Section 2, we overview the respective principles of hybrid illumination imaging and FTL in telecentric setup, and describe how to combine them to design the optical arrangement that we used to implement our proposed *in vivo* approach. In Section 3, the performance of our system is characterized and investigated using fluorescently labeled microspheres, and pollen grains. Experimental performance is further demonstrated by 3D volumetric imaging of *in vivo* Canenorhabditis elegans's (C. elegans) growth cone. Section 4 discusses advantages and limitations of our approach based on our experimental results.

2. Methods

A schematic diagram of the proposed system for *in vivo*, 3D, mechanical-scan-free, high-resolution, optically sectioned volumetric imaging is shown in Fig. 1. The excitation light is spatially modulated by the DMD, which is placed at the conjugate sample plane to produce hybrid structured pattern onto focal plane of the objective. The illuminated high-contrast structured patterns, incident at the sample plane, are detected incoherently. For focus adjustment, the FTL is utilized and located at the conjugate aperture stop of the objective in telecentric design to keep magnification and contrast constant.

Biomedical Optics EXPRESS

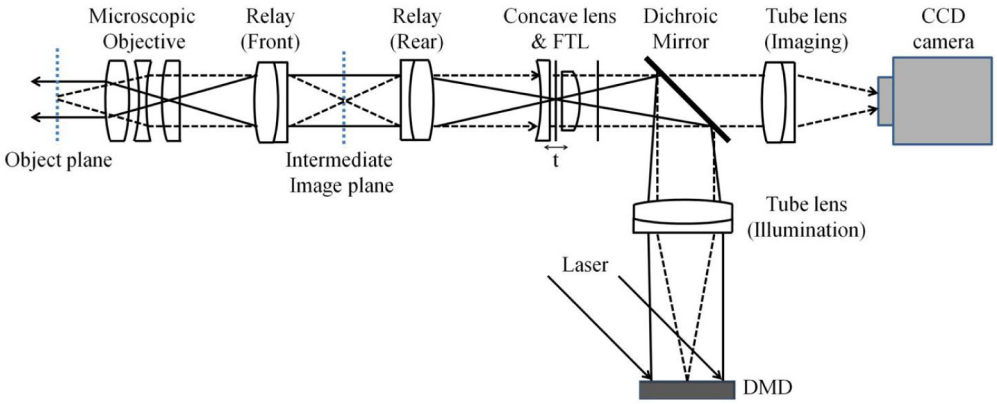

Fig. 1. Schematic drawing of the proposed microscope in epi-illumination format. In this diagram, hybrid illumination pattern from the DMD is projected onto in-focus sample plane. Focus adjustment of the excited fluorescent signal (dash line) from the sample is controlled by the FTL, which is located at the conjugate aperture stop of the objective in telecentric design to perform constant magnification and contrast.

2.1 Hybrid structured illumination for optically sectioned imaging

The principle of hybrid illumination imaging requires pair-wise fluorescence images, one with the uniform illumination image and the other standard structured illumination image, to extract an optically sectioned image at the focal plane [22–24]. The reconstructed image is the combination of the high frequency in-focus content (called *Hi* image) extracted from uniformly illuminated image and the low frequency in-focus content (called *Lo* image) extracted from combination of uniform and structured light illuminated images. The uniform illumination can be decomposed into:

$$U(x,y) = I_{in}(x,y) + I_{out}(x,y), \tag{1}$$

where $I_{in}(x,y)$ and $I_{out}(x,y)$ are in-focus and out-of-focus components. The structured illuminated image can be described similar as:

$$S(x,y) = 0.5 \cdot \left(I_{in}(x,y) \cdot \left(1 + \mu cos(2\pi f_g x)\right) + I_{out}(x,y) \right), \tag{2}$$

where μ is the modulation contrast and f_g is the spatial frequency of the imaged grid pattern. The *Hi* and *Lo* images can be written as

$$Hi = HP_{f_c}\left[U(x,y)\right], \tag{3}$$

$$Lo = LP_{f_c}\left[C(x,y) \times U(x,y)\right], \tag{4}$$

where HP and LP denote the high-pass and low-pass filters with a certain cut-off frequency f_c and the weighting function, C.

The filtered weighting function in frequency domain is obtained from multiplication of the Fourier transform of the image difference between the structured illuminated and the uniformly illuminated images with a bandpass filter, H_f.

$$C(x,y) = F^{-1}\left\{C(f_x,f_y)\right\} = F^{-1}\left\{F\left\{\left|\frac{U(x,y)}{\langle U(x,y)\rangle} - \frac{S(x,y)}{\langle S(x,y)\rangle}\right|\right\} \times H_f\right\}, \tag{5}$$

Biomedical Optics EXPRESS

where <*S*> and <*U*> represent an average of a local Gaussian low-pass filtering window in uniform and structured images, respectively. F and F^{-1} are the Fourier and inverse Fourier transform operator. H_f is the Gaussian bandpass filter to remove the noise and preserve the frequency components close to the spatial frequency of structured illumination pattern, and can be expressed as:

$$H_f\left(f_x, f_y\right) = 1 - exp\left[-\left(\frac{R\left(f_x, f_y\right) - R_0}{w \cdot R}\right)^2\right], \tag{6}$$

where R is the radial distance from the center of the filter, R_0 is the radius at the maximum value of the filter and w is the width of the bandpass filter.

The optically sectioned image can then be reconstructed as:

$$I_{sec}\left(x, y\right) = Hi\left(x, y\right) + \eta Lo\left(x, y\right), \tag{7}$$

where η is the scaling factor to obtain the seamless fusion between *Hi* and *Lo* images at the corresponding axial plane z. Typical values of η used for processing the images for our system are 0.5~3.

2.2 Telecentric design for invariant magnification

To implement mechanical-scan-free during focal adjustment, telecentric design is utilized for the insertion of the FTL [25]. Since the aperture stop of an objective is located at the rear focal point, the entrance pupil is imaged at the infinity. The magnification of the objective lens becomes invariant as a sample is moved in depth along the optical axis because the chief rays from the top of the object are parallel to the optical axis. Normally, the aperture stop of the objective lens is at inaccessible location in the microscope objective housing for FTL to form a telecentric system. Therefore, a focal relay is utilized to image the aperture stop of the objective onto the FTL. The relay lens design is symmetrical to reduce the odd aberrations and the separation between lenses has been optimized to minimize the wavefront error [26].

In addition, the FTL further incorporates a plane concave lens in the proposed system in Fig. 1 to approach symmetric focus adjustment on the sample plane. The effective lens of the FTL with the negative lens is configured at the rear focal point of the afocal relay to form a telecentric system. The effective lens power of the FTL with the negative plane concave lens can be calculated by $\phi_{FTL,eff} = \phi_{FTL} + \phi_n - \phi_{FTL} \cdot \phi_n \cdot t$, where $f = 1/\phi$. As shown in Fig. 1, t is the distance between the negative lens and the FTL. The displacement in the sample plane is denoted as Δz and the corresponding displacement in the intermediate image space is $\Delta z'$. The relationship between Δz and $\Delta z'$ is $\Delta z' = -M^2 \cdot \Delta z/n$, where M is the magnification of the objective lens with respect to the focal length of the front part of the relay lens in Fig. 1, and n is the refractive index in the sample space.

As the FTL is inserted at the rear focal point of the rear part of the relay lens, the front principal plane is shifted by distance

$$d = \frac{\phi_{FTL,eff}}{\phi_r^2}, \tag{8}$$

where ϕ_r is the lens power of the rear part of the relay lens and the displacement of the front principal plane is controlled by the effective power of FTL. According to Gaussian imagery, the object distance is increased in the minus z direction as the front principal plane is shifted toward FTL. The Δz is written as

Biomedical Optics EXPRESS

$$\Delta z = -\frac{n}{M^2}\cdot\frac{\phi_{FTL,eff}}{\phi_r^2} = -\frac{n}{M^2}\cdot\frac{f_r^2}{f_{FTL,eff}}, \tag{9}$$

where f_r and $f_{FTL,eff}$ are the focal length of the relay lens and the FTL with a negative lens, respectively.

3. Experimental results and discussion

3.1 System performance for invariant magnification and contrast during focus adjustment

The ability of the proposed fluorescence imaging microscopy based on Fig. 1, to maintain constant magnification and telecentricity during axial scanning using a FTL (EL-C-10-30-VIS-LD, Optotune), was verified by imaging a standard Air Force resolution chart (AFRC). An autofluorescent plastic slide was attached behind the AFRC such that the AFRC was able to be imaged under fluorescence condition. The imaging system with a sCMOS CCD (ORCA flash 4.0 sCMOS, Hamamatsu), had an effective system magnification of 69 × using an infinity-corrected objective lens (ULWDMSPlan100X, Olympus) with a tube lens (f = 125mm). An afocal relay system with a symmetrical configuration, consisting of two pairs of achromatic doublets (AC254-050-A1, AC254-100-A1, Thorlabs Inc.) based on telecentric design to minimize the wavefront error as described in section 2.2, was utilized between the objective lens and the combination of the FTL with a negative plane concave lens (f = −75 mm); therefore, the effective FTL is conjugate to the back aperture of the objective lens. In our proof-of-concept system, the effective focal length of FTL with the negative lens is able to be tuned from −219 mm to 77 mm with t~4 mm, and the maximum tuning range can be reached up to ~60μm based on Eq. (9). A dichroic mirror (Q505lp, Chroma Technology Corp.) and an emission filter (MF530/43, Thorlabs Inc.) were used to prevent stray excitation light from reaching the CCD camera during imaging. In Fig. 2, under uniform illumination through a DMD (DLP 6500 Texas Instruments), the smallest features (0.78 μm) on the element 3 of group 9 is clearly resolved. According to Ref [19], the focus displacement on the sample plane is linearly proportional to driven input currents (or voltages) of the FTL. In our experiment, by tuning the current of the FTL from 30 mA to 280 mA, the focus displacement is mechanically equivalent from Δz = 0 μm to 35 μm. Indeed, the focus displacement is 0.3 μm using an applied step size of 2 mA. In Figs. 2(a)-2(c), by application of different driven currents, the resultant images are obtained with corresponding mechanical displacement on the sample plane. At selected features (element 1 of group 9) on Figs. 2(a1) and 2(b1), two cross profiles are shown in Fig. 2(c) and the measured contrast is ~82% for both Δz = 0 μm and Δz = 35 μm, serving as the direct evidence of constant contrast and magnification during focus adjustment with the FTL.

Biomedical Optics EXPRESS

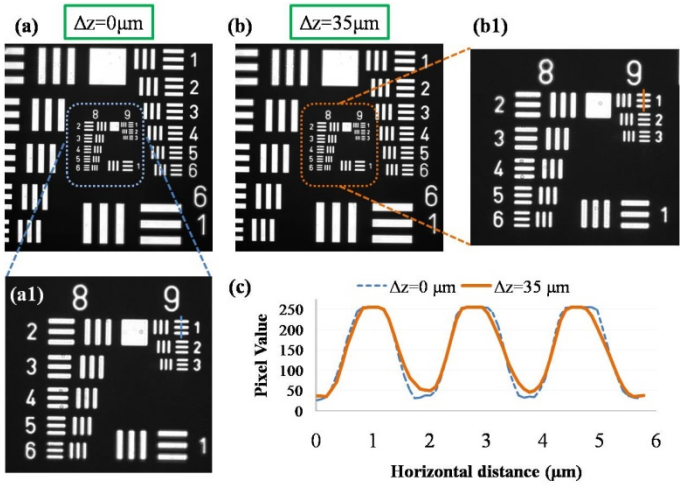

Fig. 2. AFRC obtained using the mechanical-scan-free microscope at different focal planes as an input driven current of the FTL is increased from 30mA to 280mA, (*i.e.* the focus displacement is mechanically equivalent from Δz = 0 μm to 35 μm). (c) Both cross profiles along the dash (blue) for Δz = 0 μm and solid (orange) lines for Δz = 35 μm with same contrast of ~82%.

3.2 Optical sectioning for imaging standard fluorescent samples

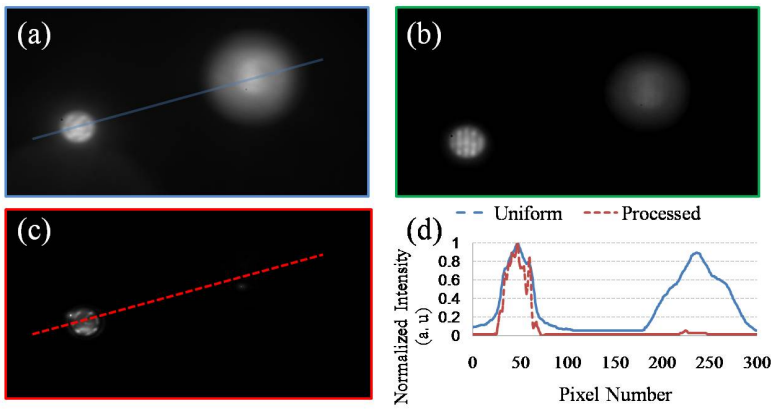

Fig. 3. (a) Uniform illuminated image, and (b) structured illumination image of 45μm fluorescent beads. (c) HiLo processed image to remove out-of-focus background using pair-wise imaging algorithm, which requires respective image of (a) and (b). (d) Intensity profiles along in-focus and out-of-focus beads. The dash (red) line indicates that the hazy background contributed from out-of-focus beads is significantly suppressed.

The optical sectioning ability of the microscope was verified by imaging fluorescently labeled 45 μm microspheres (Polysciences, Warrington, PA, USA). The microspheres, suspended in a 1 mm thick slab of agarose (Invitrogen), were excited using a blue diode laser source at λ = 473 nm. Figure 3 provides comparisons of standard wide-field and optical sectioning images captured using our proposed system under a standard uniform illumination, and DMD-based hybrid structured illumination. In Fig. 3(a), with uniform illumination the image of fluorescently labeled microspheres with out-of-focus light is captured from the CCD, which indicates poor depth selectivity. Figure 3(b) shows that the contrast of grid patterns, generated by the DMD, on the in-focus microspheres is obviously clear, while the grid pattern on the out-of-focus microspheres is barely observed. Figure 3(c) shows the resultant optical sectioning image, processed based on hybrid imaging principle in Section 2.1 by using the

Biomedical Optics EXPRESS

uniform illuminated image (Fig. 3(a)) and hybrid structured illuminated image with 54 lines-per-millimeter (lp/mm) (Fig. 3(b)) at the sample plane. The hybrid imaging principle was used to remove the out-of-focus background noise from the desired in-focus signal. In Fig. 3(d), a comparison of the uniform illumination images and the processed hybrid illumination image shows that the out-of-focus background light is suppressed significantly.

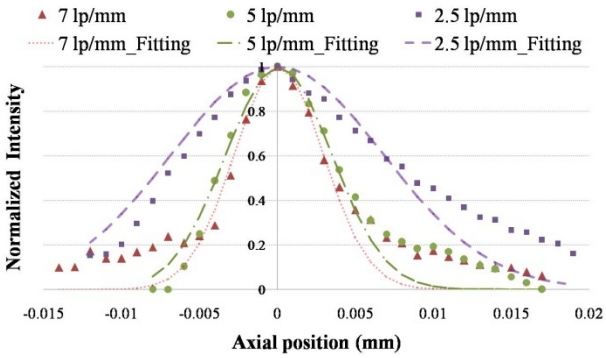

Fig. 4. The axial contrast plot of the projected structured illumination image under bright field illumination condition representing the z point spread function using hybrid computational method with different spatial frequencies of the projected grid pattern with 2.5lp/mm (marked with violet color), 5lp/mm (marked with green color) and 7lp/mm (marked with brown color), respectively.

In order to quantify the optical sectioning of the microscope, imaging contrast of the DMD projected grid with different spatial frequency was investigated and measured. The fluorescent beads' sample was scanned along the optical axis, concurrently keeping the other imaging conditions constant. Figure 4 performs the system's depth resolution in term of the grid contrast. The contrast is calculated by $(I_{max}\text{-}I_{min})/(I_{max} + I_{min})$, where I_{max} and I_{min} correspond to the intensity of the bright stripe and dark stripe of the grid pattern, respectively. The decay in the contrast of the projected grid pattern on the fluorescence microsphere along the axial direction defines the optical sectioning capability of the system [17, 27]. After Gaussian curve fitting, the respective full width half maximum (FWHM) of the grid patterns with spatial frequencies at 2.5lp/mm, 5lp/mm and 7lp/mm is 15.86, 8.2, and 6.7 μm, corresponding to 3.7, 1.9, and 1.56 μm at the sample space. Clearly, by programming the DMD to project grid pattern with higher spatial frequency on the sample plane, the system based on hybrid structured illumination offers finer optical sectioning capability in suppressing defocus background.

Biomedical Optics EXPRESS

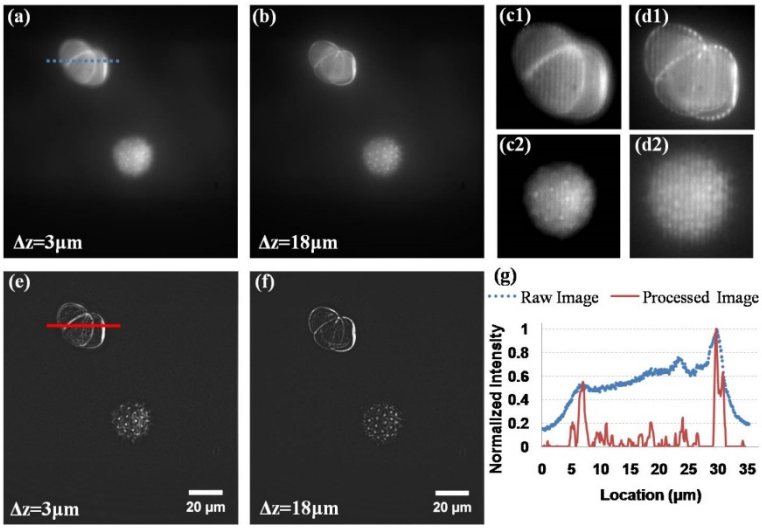

Fig. 5. (a, b) Uniform illuminated images of mixed fluorescent pollen grains at Δz = 3μm and 18 μm, respectively. (c1, c2) Zoom-in structured illuminated images of the top fluorescent pollen at respective Δz = 3μm and 18 μm. (d1, d2) Zoom-in structured illuminated images of the bottom fluorescent pollen at respective Δz = 3μm and 18 μm. (e, f) Corresponding hybrid processed images using HiLo pair-wise imaging algorithm. (g) Intensity cross-section along the dash (blue) and solid (red) lines at Δz = 3μm of the uniformly illuminated and hybrid illuminated images (a) and (e), respectively.

In addition, the microscopic system performance to resolve volumetric samples was evaluated by imaging auto-fluorescence pollen grains. Figures 5(a) and 5(b) show the images of the mixed pollen grains (Carolina, USA) under standard uniform illumination at two different depths, and haze, which is clearly observed in both depths, results from strong out-of-focus background. Figures 5(c) and 5(d) are zoomed-in pollen images with projected grid patterns at corresponding depths, respectively. Figures 5(e) and 5(f) show resultant processed images based on hybrid imaging principle. Figure 5(g) shows intensity cross-sections at Δz = 3 μm comparing the signal-to-background with uniform illumination and hybrid structured illumination. It is clear that the haze (*i.e.* background) has been suppressed significantly such that low contrast features are now visible with good signal to background ratio. The video about more depths within the pollen grains with HiLo post processing can be found in the supplement Visualization 1.

Figure 6(a) is the image of Lilium pollens with standard uniform illumination, while Fig. 6(b) further shows the resultant fusion of 65 optically sectioned images, with a step size of 0.3 μm in focus adjustment via an applied FTL step size of 2 mA, using hybrid process to provide extended depth of field.

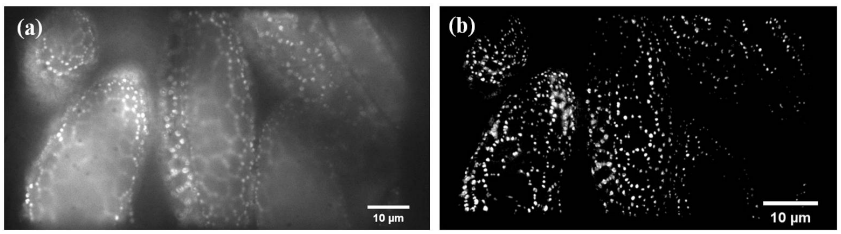

Fig. 6. (a) Uniformly illuminated image of Lillium pollens. (b) A fusion of sixty-five optically sectioned images of the pollens.

Biomedical Optics EXPRESS

3.3 Experimental result of imaging in vivo C. elegans' growth cones

To demonstrate *in vivo* imaging capability of the microscopic system, we performed an experiment to image growth cones of a live auto-fluorescence transgenic C. elegans worm. We kept a paralyzed worm with leavemisole on a microwell dish, before performing *in vivo* imaging experiment [28]. Figure 7 shows the *in vivo* images of growth cones of the worm as taken with our microscope. In Figs. 7(a1)-7(a3), images of the *in vivo* C. elegans at different depths by application of different driven currents on FTL were taken with uniform illumination, *i.e.* without projected grid pattern from the DMD. However, haze is significantly visible at all depths due to the thick nature of the sample and the standard wide-field illumination. Figures 7(d) and 7(e) are zoom in images of the boxes highlighted in Figs. 7(a2) and 7(b2) with uniform and structured illumination at the corresponding depth, respectively. The background has been suppressed significantly and low contrast features of anvil-shaped growth cones are now clearly resolved in Fig. 7(e). The video about more depths within the entire live worm with HiLo post processing can be found in the supplement Visualization 2.

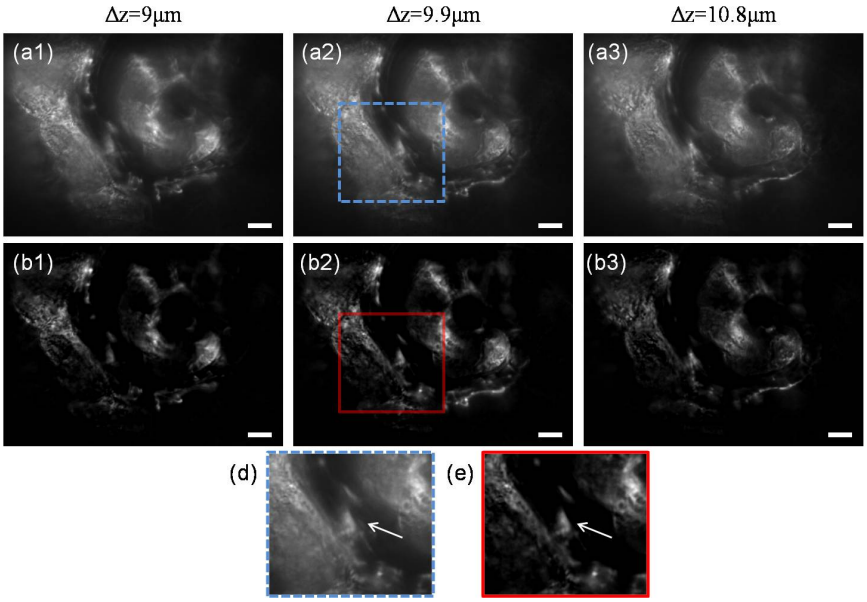

Fig. 7. (a1-a3) Uniform illuminated images of a transgenic C. elegans worm at three different depths. (b1-b3) Corresponding hybrid processed images using HiLo pair-wise imaging algorithm at three depths, respectively. (c, d) Zoom-in to the solid-box and dashed-box regions of (a2), and (b2), respectively. Scale bars are 10μm in length.

4. Conclusion

We have developed an *in vivo*, mechanical-scan-free, multi-plane, wide-field optical sectioning microscope for 3D volumetric imaging of biological samples. Image contrast and operation speed are achieved from a combination of programmable DMD based hybrid illumination imaging and FTL with invariant imaging magnification formation. The proposed microscope is simple, fast, and robust to observe *in vivo* images from different planes within a volumetric biological simple while effectively rejecting out-focus-background. Although the amount of spherical aberration may increase linearly with the scanning depth at normal incidence [29], the aberration can be minimized using an additional FTL or adaptive optics to further correct wavefront error. In addition, it is possible to speed up the post-process through a faster computation device, such as a graphic processing unit (GPU), to reconstruct 3D images in real time.

Biomedical Optics EXPRESS

Acknowledgments

The authors gratefully acknowledge Dr. Pei-Hsin Huang, Dr. Hwai-Jong Cheng for providing biological samples, and the support from the following sponsors: and Taiwan Ministry of Science and Technology (103-2221-E-002-156-MY3, 105-2628-E-002-008-MY3), National Health Research Institutes (EX104-10220EC), National Taiwan University (105R7808), and National Taiwan University Hospital (UN105-033). Authors C. Lin, and J. Tsai contributed equally to this work.